Article

Not peer-reviewed version

An Improved IHBA-BP Neural Network for Temperature Compensation of Load Cells

Zhen-Jie Zhang , Wan-Sheng Cheng * , Dai-Xing Zhang

Posted Date: 11 May 2026

doi: 10.20944/preprints202605.0664.v1

Keywords: temperature compensation; load cell; IHBA-BP model; experimental calibration system

Article

An Improved IHBA-BP Neural Network for Temperature Compensation of Load Cells

Zhen-Jie Zhang [1,2], Wan-Sheng Cheng [1,*] and Dai-Xing Zhang [2]

[1] School of Electronic and Information Engineering, University of science and technology Liaoning, Liaoning Anshan, 114051, People's Republic of China

[2] School of Mechanical Engineering and Automation, University of Science and Technology Liaoning, Anshan City, Liaoning Anshan, 114051, People's Republic of China

* Correspondence: cws@ustl.edu.cn

Highlights

What are the main findings?

- An improved Honey Badger Algorithm (HBA) with adaptive parameters and a stagnation aware strategy is proposed to enhance global optimization performance.
- The improved algorithm is applied to optimize the BP neural network for temperature compensation of load cells.

What are the implications of the main findings?

- The proposed method significantly improves compensation accuracy compared with existing approaches, as demonstrated by experimental results.

Abstract

During the measurement process, load cells are susceptible to temperature variations, which can significantly degrade measurement accuracy. To address this problem, this paper presents a temperature compensation method based on an improved neural network. First, the mechanism of sensor temperature drift is analyzed from a thermodynamic perspective. Subsequently, an Improved Honey Badger Algorithm (IHBA) is developed to optimize the initial weights and biases of a Back-Propagation (BP) neural network, aiming to enhance global search capability and convergence stability. To validate the proposed method, a dedicated calibration experimental system was constructed, and temperature-dependent output data were collected over a range of 0 °C to 60 °C. Comparative experiments with conventional methods, including IMA-BP, PSO-BP, standard BP, and polynomial fitting, were conducted. In addition, an ablation study was performed to verify the effectiveness of the proposed improvements. The results demonstrate that the IHBA-BP model achieves superior compensation performance. The temperature drift coefficient and sensitivity temperature coefficient are reduced by 86.6% and 95.86%, respectively. The proposed method shows strong potential for improving measurement accuracy of load cells under varying temperature conditions and provides a practical solution for industrial sensor calibration applications.

Keywords: temperature compensation; load cell; IHBA-BP model; experimental calibration system

1. Introduction

The fields of aerospace, advanced manufacturing, and metallurgical industries [1–3], the precise control of machining forces is the key to ensuring product quality, which relies on high-precision load cells. However, the measurement results of classical strain-gauge load cells are susceptible to various external environmental factors, such as electromagnetic interference, temperature variations, and mechanical fatigue [4–6]. Among these, temperature variation exerts the most significant influence. The zero drift and sensitivity drift induced by temperature variations can severely degrade the measurement accuracy of the sensor [7].

At present, temperature compensation methods for sensors are divided into two parts: hardware compensation and software compensation [8,9]. Hardware compensation includes the bridge circuit compensation method, resistor compensation and diode compensation [10,11]. However, hardware compensation suffers from high costs and poor flexibility. Particularly when compensating over a wide temperature range, it often fails to deliver satisfactory results [12].

Comparing with the hardware approaches, software-based compensation offers lower cost and greater flexibility. Software compensation methods include: curve interpolation method, polynomial fitting method [13], multi-dimensional regression method [14] and least squares support vector machine (LSSVM) algorithm [15]. However, these methods exhibit certain limitations in temperature compensation applications. Curve interpolation and polynomial fitting methods are prone to overfitting when applied to sensor temperature compensation. The multi-dimensional regression method imposes strict requirements on the accuracy of the predefined functional form. In addition, LSSVM and least squares surface fitting methods may require considerable computational resources during implementation.

Owing to their capability in modeling complex nonlinear relationships, neural networks have been widely applied to sensor temperature compensation. Futane et al. [16] applied an Artificial Neural Network (ANN) algorithm to compensate for pressure sensor temperature drift. The network learned the nonlinear mapping between temperature and sensor output from experimental data, adjusting weights and thresholds iteratively to reduce compensation error. Zhang et al. [17] employed a Back Propagation (BP) neural network for strain sensor compensation. They found the temperature-induced error reduced significantly. Subsequently, Pang et al. [18] proposed a temperature compensation method based on Radial Basis Function (RBF) neural network.

Although neural networks can achieve high compensation accuracy, their dependence on initial weights and thresholds, as well as their susceptibility to local optima, may restrict robustness and stability. To alleviate these limitations, researchers have introduced metaheuristic algorithms to optimize neural network parameters.

Due to its simplicity and effectiveness, Particle Swarm Optimization (PSO) [19] has been extensively used for neural network optimization. Gordan et al. [20] proposed a PSO-optimized ANN for sensor applications. They demonstrated that the convergence of the PSO-ANN is better than that of the ANN. Wu et al. [21] demonstrated that the PSO-RBF network achieved better temperature compensation performance than the unoptimized RBF model.

Nevertheless, PSO may suffer from premature convergence and parameter sensitivity, potentially affecting compensation stability. Consequently, increasing attention has been devoted to recently developed metaheuristic strategies. For example, Wang et al. [22] proposed a temperature compensation scheme for a multi-channel pressure scanner, where an improved Cuckoo Search (CS) algorithm [23] was employed to optimize the BP neural network. The Black Widow Optimization (BWO) algorithm was applied to optimize a BP network for fiber optic sensor temperature compensation by Li et al. [24]. Subsequently, Wang et al. [25] applied a genetic algorithm optimized-BP neural network to temperature-compensate a MEMS resonant accelerometer. Li et al [26] employed the ISSA-BP neural network to mitigate the influence of the temperature drift on the sensor output. Furthermore, the Long-Short Term Memory (LSTM) [27] and the PSO-LSSVM method [28] were also used to perform temperature compensation.

The performance of metaheuristic-optimized models largely depends on the characteristics of the selected optimization algorithm. However, many existing metaheuristic strategies still face challenges such as limited global search capability, parameter sensitivity, and slow convergence. These factors may affect compensation stability and measurement reliability. An effective optimization algorithm should maintain adequate global exploration capability to avoid local optima while preserving computational efficiency and practical deployability across different sensing systems.

The Honey Badger Algorithm (HBA), proposed by Hashim et al. in 2022 [29], is a recently developed metaheuristic inspired by the foraging behavior of honey badgers. It features a balance between exploration and exploitation, strong global search capability, and relatively few adjustable parameters. These characteristics make it a promising candidate for optimizing neural network-based temperature compensation models. Therefore, this study adopts HBA to optimize a BP neural network for load cell temperature compensation.

Unlike existing studies that mainly focus on algorithmic optimization itself, this work is motivated by the practical requirement of improving temperature compensation accuracy under real calibration conditions of industrial load cells. The proposed IHBA-BP model is designed not only to enhance optimization capability, but also effectively compensates for measurement errors induced by temperature drift in the experimental system.

This paper is organized as follows. In Section II, the reason for the temperature drift is analyzed. The temperature compensation method, which consists of the BP Neural Network and the IHBA, is established in Section III. Then, Section IV introduces the experimental test system for the load cell. Subsequently, the test results are analyzed using the proposed temperature compensation method in Section V. Finally, Section VI presents the conclusion.

2. Temperature Drift of a Load Cell

For a strain gauge, the relationship between the resistance value of the resistance strain gauge and temperature can be expressed as:

$$R_t = R_0\left(1+\alpha_0\Delta t\right) \tag{1}$$

where, R_t and R_0 represent the resistance value of the strain gauge at temperatures t and 0 degrees respectively. α_0 represents the resistance temperature coefficient of the strain gauge resistance wire. Δt is the temperature difference. When the temperature changes by Δt, the change in resistance of the strain gauge is given by Equation (2).

$$\Delta R_\alpha = R_t - R_0 = R_0\alpha_0\Delta t \tag{2}$$

In a strain gauge load cell, the principle of thermal expansion means that changes in ambient temperature cause synchronous dimensional changes in both the elastomer and the strain gauge. When the sensor's elastomer and the strain gauge strain gauge resistance wire have the same coefficient of thermal expansion, changes in ambient temperature will not cause additional deformation. However, due to the difference in their coefficients of thermal expansion, the elastomer and the strain gauge undergo unequal dimensional variations under the same temperature change.

Let the lengths of the strain gauge resistance wire and the elastomer both be L_0 at a temperature of 0 degree. Their coefficients of thermal expansion are β_s and β_g respectively. If the strain gauge is not attached to the elastomer, the lengths of the resistance wire L_s and the elastomer L_g are shown as:

$$\begin{aligned} L_s &= L_0\left(1+\beta_s\Delta t\right) \\ L_g &= L_0\left(1+\beta_g\Delta t\right) \end{aligned} \tag{3}$$

If the strain gauge is attached to the elastomer, the additional deformation ΔL, the additional strain ε_β and the additional resistance ΔR_β of the strain gauge resistance wire are shown as:

$$\begin{aligned} \Delta L &= L_g - L_s = \left(\beta_g - \beta_s\right)L_0\Delta t \\ \varepsilon_\beta &= \frac{\Delta L}{L_0} = \left(\beta_g - \beta_s\right)\Delta t \\ \Delta R_\beta &= KR_0\varepsilon_\beta = KR_0\left(\beta_g - \beta_s\right)\Delta t \end{aligned} \tag{4}$$

The relative change in the total resistance of the resistance strain gauge caused by temperature is:

$$\frac{\Delta R_t}{R_0}=\frac{\Delta R_\alpha+\Delta R_\beta}{R_0}=\left[\alpha_0+K\left(\beta_g-\beta_s\right)\right]\Delta t \tag{5}$$

The strain caused by changes in environmental temperature is given as Equation (6). This phenomenon is called zero temperature drift.

$$\varepsilon_t=\frac{\Delta R_t/R_0}{K}=\left[\frac{\alpha_0}{K}+\left(\beta_g-\beta_s\right)\right]\Delta t \tag{6}$$

The zero-temperature coefficient γ_0 is a parameter that quantifies how much the sensor's zero-point drifts with temperature, as defined in Equation (7).

$$\gamma_0=\frac{U_T-U_{T_0}}{U_{FS0}\left(T-T_0\right)}\times10^6 \quad (\text{ppm/°C}) \tag{7}$$

where U_T is the no-load output voltage under at temperature T; U_{T0} is the no-load output voltage under at temperature T_0 and U_{FS0} is the full load output voltage at T_0.

The input-output characteristic of the load cell also varies with temperature, a phenomenon known as sensitivity temperature drift.

The sensitivity temperature coefficient γ_s quantifies the change in the sensor's sensitivity with temperature, which is given by:

$$\gamma_s=\frac{S_T-S_{T_0}}{S_{T_0}\left(T-T_0\right)}\times10^6 \quad (\text{ppm/°C}) \tag{8}$$

where, S_T is the sensitivity measured at the specific temperature under T, and S_{T0} is the sensitivity at the reference temperature T_0.

Zero temperature drift and sensitivity temperature drift collectively form temperature drift [30].

3. Temperature Compensation

The principle of a load cell temperature compensation is shown in the Figure 1. The measured force F and measured temperature T are the input values, and the compensation predicted force F' is the output value.

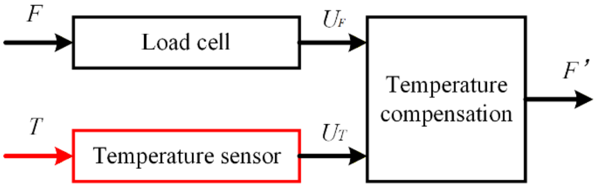

Figure 1. The principle of a load cell temperature compensation.

3.1. BP Neural Network

BP Neural Network is a multi-layer feedforward neural network based on the error backpropagation algorithm. BP neural networks are widely used in classification, regression, pattern recognition, and other fields. Their core idea lies in adjusting the weights and bias parameters, thereby enabling the network to approximate any complex nonlinear function. Given the characteristics of the BP neural network, it was selected as the kernel algorithm for temperature compensation of a load cell.

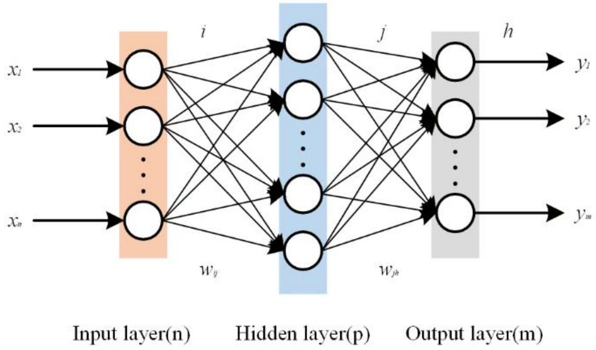

Figure 2. Basic structure of a practical 3-layer BP neural network.

Figure 2 shows the basic structure of a practical 3-layer BP neural network. It consists of three parts: the input layer, the hidden layer, and the output layer. Each node represents a neuron. The working mechanism of the BP neural network is primarily divided into two stages: forward propagation and backward propagation.

Forward Propagation: The input signals are processed through a weighted sum and passed to the nodes in the next layer via an activation function, ultimately yielding an output result, as shown in Equation (9). In Equation (9), w_{ij} represents the weights, and b_j denotes the bias. If the error between the output result and the expected value exceeds a predefined threshold, the process proceeds to the backward propagation stage. The error between the output and the expected value is calculated using Equation (10). In order to determine whether the compensation is effective, $y(h)$ is used as predicted force, and $y_n(h)$ is used as calibrated force in the temperature compensation model.

$$x_j = \sum_i \omega_{ij} x_i + b_j \tag{9}$$

$$E = \frac{1}{2}\left[y(h) - y_n(h)\right]^2 \tag{10}$$

Backward propagation: The error at the output layer is calculated and propagated backward through the network to the hidden layer. The connection weights of each layer are then updated using the gradient descent method to minimize the overall error.

The initial weights and biases of the BP neural network are typically assigned randomly, which may lead to an uneven distribution of candidate solutions within the search space. As a result, the network may converge prematurely without adequately exploring the global optimum region. To alleviate this limitation, a metaheuristic algorithm with strong exploration capability, namely the Honey Badger Algorithm (HBA), is introduced to optimize the BP neural network. The initial weights and biases are determined through the search process of HBA, thereby enhancing the global search ability and improving optimization efficiency.

3.2. Improvement of HBA

The Honey Badger Algorithm (HBA) is inspired by the honey badger's foraging strategies: digging and following honeyguide birds. These correspond to the algorithm's digging mode and honey mode. In digging mode, the honey badger uses its sense of smell to locate prey and then moves around to select a digging spot. In honey mode, it directly locates prey by following the honeyguide bird. The detailed steps of the HBA are as follows:

Step 1: Initialization phase. Initialize the position of each honey badger based on Equation (11).

$$x_i = lb_i + r_1 \times (ub_i - lb_i) \tag{11}$$

where, x_i represents the initial position of the ith honey badger. lb_i is the lower bounds. ub_i is upper bounds. r_1 is a random number in the range ($0 < r_1 < 1$). i represents dimensionality.

Step 2. Defining intensity (I)

Intensity is related to the concentration of prey and the distance between the prey and the honey badger. The more concentrated the prey and the closer the distance between the honey badger and the prey, the greater I, as expressed by Equation (12).

$$I_i = r_2 \times \frac{S}{4\pi d_i^2} \tag{12}$$

$$S = \left(x_i - x_{i+1}\right)^2 \tag{13}$$

$$d_i = x_{prey} - x_i \tag{14}$$

where, d_i is the distance between the prey and the ith badger. r_2 is a random number between 0 and 1. S denotes source strength or concentration strength.

Step 3. Update density factor.

The density factor α is given by Equation (15). It is used to balance exploration and exploitation.

$$\alpha = C \times \exp\left(\frac{-t}{t_{\max}}\right) \tag{15}$$

where, C is a constant which is greater than 1. t is the current number of iterations. t_{max} is the maximum number of iterations.

Step 4. Update position.

In the previous discussion, HBA is divided into digging phase and honey phase.

3.2.1. Digging Phase

The motion of digging phase is calculated by:

$$x_{new} = x_{prey} + G \times \beta \times I \times x_{prey} + G \times r_3 \times \alpha \times d_i \times \left[\cos\left(2\pi r_4\right) \times \left[1 - \cos(2\pi r_5)\right]\right] \tag{16}$$

where, x_{prey} is the global optimal point. G is used as a flag that alters the movement direction of the honey badger, it is determined in Equation (17). β represents the ability to search for food ($\beta \geq 1$). r_3, r_4, and r_5 are three random numbers between 0 and 1.

$$G = \begin{cases} 1 & if, r_6 \leq 0.5 \\ -1 & else \end{cases} \tag{17}$$

where, r_6 is a random number between 0 and 1.

3.2.2. Honey Phase

The motion of a honey badger following a honeyguide bird to a beehive is described by:

$$x_{new} = x_{prey} + G \times r_7 \times \alpha \times d_i \tag{18}$$

where, r_7 is a random number between 0 and 1. x_{prey} represents the best candidate solution found thus far, which may be a local optimum rather than the global one. Employing a perturbation factor r_7 is essential to facilitate escape from local optima and enhance the exploration toward the global best position.

To meet the demands of temperature compensation for both rapid convergence and extensive global search, the HBA algorithm is improved as follows.

1. The MATLAB's unifrnd function is employed to initialize the population of HBA, resulting in a more uniform initial distribution and enhancing the initial search efficiency.

2. A weight factor g is considered in the digging phase, as described in Equation (19) and Equation (20). The value of g nonlinearly decreases from 0.9 to 0.2. g allows the algorithm to emphasize exploration in the early stages, whereas its intensity is reduced later on, thereby promoting a more refined search and preventing excessive disturbances in the later phase.

doi:10.20944/preprints202605.0664.v1

$$x_{new} = x_{prey} + g \times G \times \beta \times I \times x_{prey} + G \times r_3 \times \alpha \times d_i \times \left[\cos\left(2\pi r_4\right) \times \left[1 - \cos(2\pi r_5)\right]\right] \tag{19}$$

$$g = g_{\max} - \left(g_{\max} - g_{\min}\right)\exp(-5\frac{t}{t_{\max}}) \tag{20}$$

3. The Lévy flight strategy is applied to the honey phase [31], as determined in Equation (21). Due to its occasional long-distance jumps, Lévy flight strategy can significantly enhance the global exploration ability and help escape local optima effectively. Meanwhile, an adaptive improvement is made to the characteristic exponent β of Lévy flight. At the beginning of iterations, β is set to a small value ($\beta = 1.2$), and later increases to large value ($\beta = 1.8$). The new position of honey badger can be redefined as Equation (22).

$$Levy = \frac{u \times \sigma}{|v|^{-\beta}} \tag{21}$$

$$x_{new} = x_{prey} + Levy \times F \times \alpha \times d_i \tag{22}$$

4. The triggering probability of the honey phase is increased. During the mid-to-late stages of HBA iteration, if convergence stagnation is detected (e.g., the best solution remains unchanged for 5 or 10 consecutive iterations), this probability is raised.

The above improvements are designed to enhance the balance between global exploration and local exploitation. The nonlinear weight factor mainly improves early-stage exploration, whereas the Lévy flight strategy increases the probability of escaping local optima. The adaptive triggering mechanism further stabilizes convergence in the later stage. These improvements jointly contribute to a more robust optimization process

3.3. IHBA-BP

Temperature compensation for the load cell is carried out using the IHBA-BP neural network. The optimal weights and biases of the sample data need to be calculated using IHBA. The dimensionality of the algorithm is equal to the total number of weights and biases. The optimal weights and biases obtained by IHBA are used as the initial weights and biases of BP. It can improve the convergence precision, and shorten search time. Finally, the gradient descent method is used to further optimize the compensated results and further improve the compensation accuracy. The specific algorithm flow chart is shown in Figure 3.

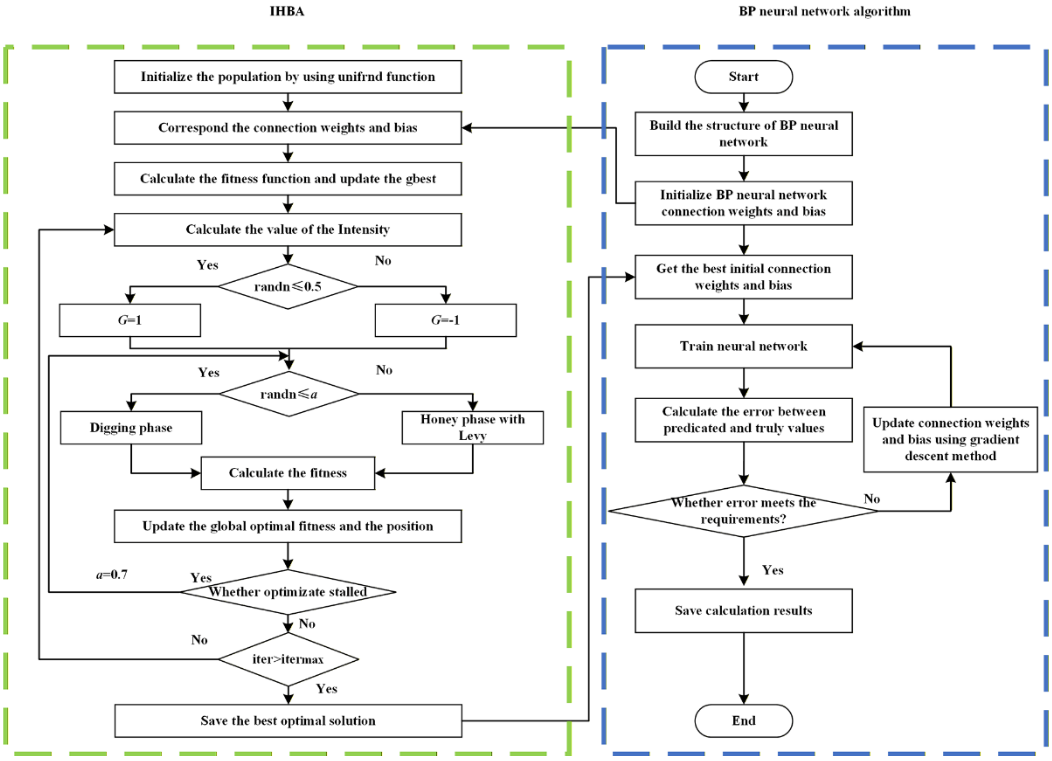

Figure 3. Flow chart.

4. Calibration Experimental System

To investigate the output characteristics of the load cell under different temperatures and to perform thermal compensation, a calibration experimental system was built in this paper. The load cell experimental calibration system consisted of experimental test system, load cell module and strain gauge adhesive device.

4.1. Experimental Test System

The building experimental test system includes: temperature control system, data collection system and loading system, which is shown in Figure 4.

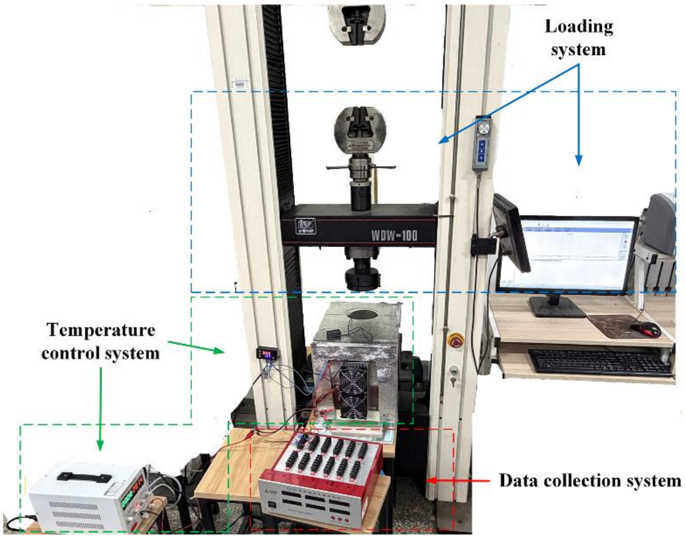

Figure 4. Experimental test system.

A temperature control system capable of real-time adjustment was designed to measure the output signal of the elastomer at different temperatures. The system consists of a heating module, a cooling module, a temperature control module, and a constant temperature chamber. The heating module employed a PTC component, and the cooling module utilizes a semiconductor refrigeration component, as illustrated in Figure 5 (a). For precise temperature regulation, a W3230 high-precision temperature controller was adopted. All modules were mounted on the constant temperature chamber, which was constructed with polyurethane insulation material and wrapped externally with heat-reflective aluminum foil to minimize heat exchange with the ambient air, as shown in the Figure 5 (b).

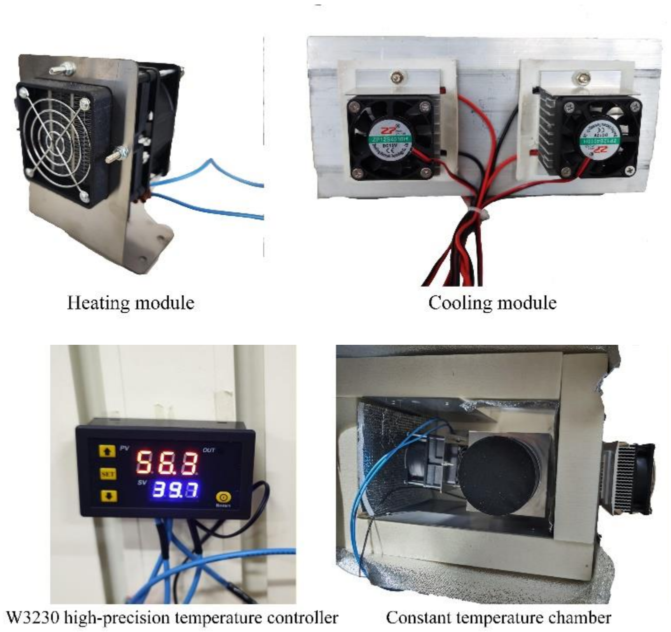

(a) (b)

Figure 5. Temperature control system. (**a**) Heating and Cooling module. (**b**) Constant tempera-ture chamber.

The load cell measurement circuit was configured as a full-bridge circuit, and the tests were conducted using an XL2101C static strain gauge. The XL2101C static strain gauge is shown in Figure 6. The measurement range of the instrument is -19999 to +38000 με, and the resolution is 1 με. The bridge excitation voltage is 2 V.

Figure 6. XL2101C static strain gauge.

The loading system employed a calibrated 0.5-grade hydraulic universal testing machine, WDW-100, as the standard force source. The device is shown in Figure 7. This device has a maximum load capacity of 100 kN. WDW-100 has an accuracy class of 0.5, meaning its indication error is within ±0.5% of the full scale. This level of accuracy represents a common configuration in many industrial settings and typical laboratory environments.

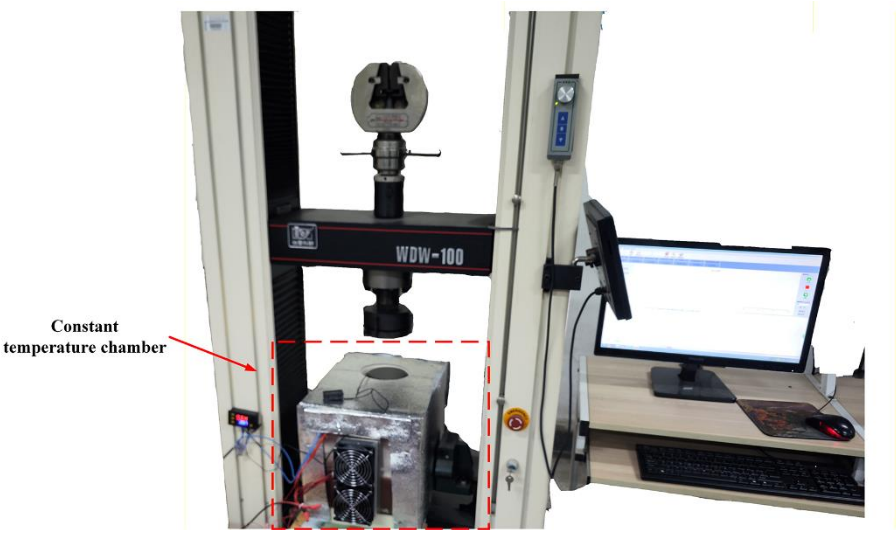

Figure 7. WDW-100 electronic universal testing machine.

4.2. Load Cell Elastomer

The elastomer was secured with a dedicated fixture to prevent movement, as shown in Figure 8. To ensure thermal insulation and avoid temperature influence from the press head, an insulating block made of force resistant ceramic was placed between the press head and the fixture, effectively blocking heat transfer. The elastomer was fabricated from 7075 T6 aluminum alloy, which has an elastic modulus of 71 GPa and a yield strength of 445 MPa. To minimize random errors, three identical elastomers were manufactured, and the experimental results reported are the average of the measurements from all three.

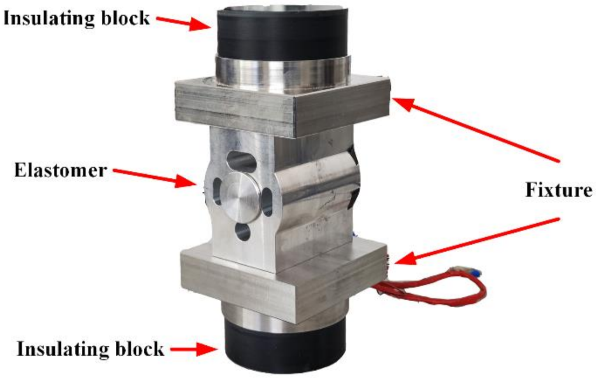

Figure 8. Load cell elastomer.

4.3. Strain Gauge Adhesive Device

To enable the bonding of strain gauges inside elastomer's center hole, this paper presents a novel strain gauge adhesive device, as shown in Figure 9. Based on a linkage mechanism, the device converts the axial motion of a central shaft into the radial horizontal movement of the strain gauge. This action ensures the strain gauge was applied evenly onto the inner wall of the elastomer's center hole.

Figure 9. Strain gauge adhesive device.

5. Results and Discussion

5.1. Experiment Results

The output signals of the elastomer were measured on the calibrated test bench over a temperature range of 0 °C to 60 °C. To ensure accuracy, the system was heated and held at each target temperature for 30 min to reach thermal equilibrium before applying load to the elastomer. The load was maintained for 5 seconds before recording the output reading. To eliminate random errors, three repeated tests were performed on each of the three fabricated elastomers. The final result was the average of these nine measurements. The training set presented in Table 1 are the averaged values.

Table 1. Training set.

Temperature (°C)	**U (mV)**					
	0kN	**10kN**	**20kN**	**30kN**	**40kN**	**50kN**
0	0.011	0.6083	1.2067	1.8029	2.4024	2.9953
5	0.0044	0.6105	1.2177	1.8194	2.4189	3.025
10	-0.0055	0.6061	1.2122	1.8227	2.4299	3.0382
15	-0.0011	0.6171	1.2177	1.8271	2.4343	3.0415
20	0	0.6149	1.2221	1.8348	2.4431	3.0525
25	-0.0121	0.6061	1.221	1.8348	2.4519	3.0624
30	-0.0132	0.6028	1.2166	1.8293	2.4442	3.0547
35	0.0055	0.6149	1.2221	1.8238	2.431	3.0382
40	0.0165	0.6248	1.2254	1.8304	2.4376	3.036
45	0.0286	0.6336	1.2287	1.8326	2.4343	3.0327
50	0.0187	0.6237	1.2276	1.8304	2.4343	3.0338
55	0.0099	0.6116	1.2133	1.8161	2.4167	3.0129
60	0.0033	0.6083	1.2089	1.8106	2.4123	3.0096

For load cells, the measurement value at 20 °C is typically used as the calibration reference. Accordingly, the static strain gauge was zero-calibrated at 20 °C prior to the experiment.

To comprehensively evaluate the performance of the subsequent temperature compensation algorithm, in addition to the relative error e_r, three other evaluation metrics are introduced: full-scale error e_f, mean square error (MSE), and root mean square error (RMSE). Their definitions are provided in Equation (23).

$$\begin{cases} e_r = \max\left|U_r - \hat{U}_r\right|, r = 1,2,\ldots,N \\ e_f = \max\left(\dfrac{\left|U_r - \hat{U}_r\right|}{U_{FS}}\right)\times 100\%, r = 1,2,\ldots,N \\ MSE = \dfrac{1}{N}\sum_{i=1}^{N}\left(U_r - \hat{U}_r\right)^2, r = 1,2,\ldots,N \\ RMSE = \sqrt{\dfrac{1}{N}\sum_{i=1}^{N}\left(U_r - \hat{U}_r\right)^2}, r = 1,2,\ldots,N \end{cases} \tag{23}$$

where, U_r is the measured voltage, $\hat{U}_r$ is the calibrated voltage under the reference condition (20 °C), U_{FS} is the voltage corresponding to the full-scale output, N is the number of measurement points.

5.2. Analysis of Compensation Results

For the IHBA-BP neural network, the IHBA optimizer was configured with a population size of 100 and a maximum iteration count of 1000, along with parameters $\beta = 6$ and $C = 2$. The BP network consisted of one hidden layer which contains six neurons. The hyperbolic sine function was employed as the activation function between the input layer and the hidden layer. Considering that the load cell output is normalized within a bounded range, the Sigmoid activation function is adopted in the output layer to better capture the nonlinear mapping characteristics and ensure stable output within the valid range. The compensation results are illustrated in Figure 10.

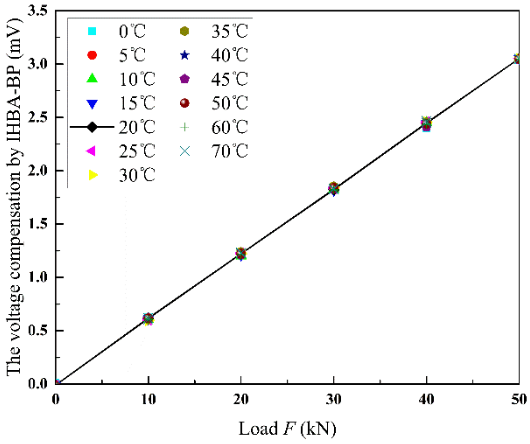

Figure 10. The compensation results by IHBA-BP.

To comprehensively evaluate the performance of the proposed IHBA-BP, its compensation results are compared with those obtained from five established methods: a Particle Swarm Optimized BP neural network (PSO-BP), an improved Mayfly algorithm Optimized BP neural network (IMA-BP) [32], a standard BP neural network (BP), and a polynomial fitting method. Furthermore, to further evaluate the effectiveness of each improvement in IHBA, an ablation study was conducted by comparing the proposed method with its simplified variants.

The compensation results obtained using different methods are presented in Table 2. Compared with the raw uncompensated data, the temperature drift coefficient of the sensor was reduced by 86.6% after IHBA-BP compensation, and the sensitivity temperature coefficient was reduced by 95.86%, both of which satisfy the design specifications. In comparison with typical existing compensation methods, such as PSO-BP, BP and polynomial fitting, the proposed IHBA-BP model demonstrates significant advantages in terms of temperature drift coefficient, sensitivity temperature coefficient, and various error metrics. The results also showed that each modification contributes to performance improvement, and the complete IHBA achieves the best results.

Table 2. Calibration data at full temperature.

	γ0 (ppm/℃)	**γs (ppm/℃)**	**er**	**ef %**	**MSE**	**RMSE**
Experiment	374.8	936.94	0.057	1.87	2.78e-4	0.017
HBA-BP	342.64	478.8	0.084	2.74	0.0012	0.035
IHBA(no Levy)-BP	117.3	49.35	0.028	0.93	4.7e-5	0.0069
IHBA(no g)-BP	102.99	101.45	0.0174	0.57	4.35e-5	0.0066
IHBA-BP	35.09	45.75	0.0166	0.54	2.66e-5	0.005
IMA-BP	177.06	246.62	0.019	0.62	3.87e-5	0.006
PSO-BP	80.83	70.71	0.0178	0.58	3.13e-5	0.0056
BP	47.51	115.19	0.018	0.6	4.02e-5	0.0063
Polynomial Fitting	257.85	254.89	0.02	0.65	5.1e-05	0.0071

5.3. Test Results after Compensation

To further validate the effectiveness of the proposed IHBA-BP compensation model, the compensation model was applied to compensate the test set, as shown in Table 3. The corresponding compensation results are presented in Table 4.

Table 3. Experiment results.

Temperature (℃)	**U (mV)**					
	0kN	**10kN**	**20kN**	**30kN**	**40kN**	**50kN**
27	-0.0125	0.6048	1.2192	1.8326	2.4488	3.0593
37	0.0099	0.6189	1.2234	1.8264	2.4336	3.0373
47	0.0246	0.6296	1.2283	1.8317	2.4343	3.0331
57	0.0073	0.6103	1.2115	1.8139	2.4149	3.0116

Table 4. Compensation results after IHBA-BP.

Temperature (℃)	**U (mV)**					
	0kN	**10kN**	**20kN**	**30kN**	**40kN**	**50kN**
27	-0.0038	0.6076	1.217	1.8289	2.4552	3.05
37	-0.0009	0.6122	1.2233	1.8245	2.4418	3.0496
47	0.0022	0.6187	1.2327	1.8397	2.4508	3.0495
57	-0.0005	0.6119	1.2191	1.8345	2.4387	3.0485

Substituting the compensation results in Table 4 into (23), the following error metrics were obtained: e_r = 0.01207, MSE = 2.8376E-05, and RMSE = 0.005327. The full-scale error is significantly reduced compared with the uncompensated case. Specifically, e_f is reduced by 78.6%, indicating that the proposed IHBA-BP model effectively suppresses temperature-induced errors. The results demonstrate that the model achieves an accuracy level close to the instrument's full-scale specification and maintains strong temperature compensation capability on the test set, showing promising potential for engineering applications.

6. Conclusions

This paper presents a temperature compensation method to reduce the temperature drift of load cells. The proposed method is developed based on the BP neural network. To accurately capture the complex nonlinear relationship between temperature and load cell output, the BP neural network was optimized using an Improved Honey Badger Algorithm (IHBA), which enhances global search capability and provides optimal initial weights and thresholds for the network. The results show that after IHBA-BP compensation, the zero temperature drift coefficient of the load cell is reduced from

374.8 ppm/°C to 35.09 ppm/°C, and the sensitivity temperature coefficient is reduced from 936.94 ppm/°C to 45.75 ppm/°C. Compared with IMA-BP, PSO-BP, BP, and polynomial fitting methods, the IHBA-BP model yields the lowest compensation error among the evaluated approaches, indicating improved resistance to temperature-induced variations in the measurement output. Furthermore, the test results indicate a significant reduction in full-scale error, with an overall improvement of 78.6% compared with the uncompensated condition. This demonstrates that the proposed method achieves an accuracy level close to the instrument's full-scale specification and maintains high compensation performance, showing strong potential for practical engineering applications.

Author Contributions: For research articles with several authors, a short paragraph specifying their individual contributions must be provided. The following statements should be used "Conceptualization, Z. Z. and W. C.; methodology, Z. Z.; software, Z. Z.; validation, D. Z.; investigation, Z. Z.; resources, W. C.; data curation, Z. Z.; writing—original draft preparation, Z. Z.; writing—review and editing, W. C. All authors have read and agreed to the published version of the manuscript.

Funding: This research received no external funding.

Institutional Review Board Statement: Not applicable.

Informed Consent Statement: Not applicable.

Data Availability Statement: All data generated or analyzed during this study are included in this

published article.

Acknowledgments: The authors would like to thank the experiment center of University of Science and Technology Liaoning for the sincere cooperation in providing facilities.

Conflicts of Interest: The authors declare no conflicts of interest.

References

1. Huang, J.; Qiu, C.; You, Y.; Li, H. Intelligent dynamic force loading algorithm for aerospace rudder load simulator. *J. Aerosp. Eng*. **2023**, 36, 04023060. 10.1061/JAEEEZ.ASENG-4466
2. Han, X. H.; Shi, F. X.; Zhuang, W. H.; Hua, L.; Zheng, F. Y.; Xu, M. A novel multi-DOF point envelope forming process for manufacturing thin-walled components. *J. Manuf. Process*. **2025**, 134, 1082-1095. 10.1016/j.jmapro.2025.01.017
3. Bathelt, L.; Scurk, M.; Djakow, E.; Henke, C.; Trächtler, A.; Lo, W. L. Novel straightening-machine design with integrated force measurement for straightening of high-strength flat wire. *Sensors*. **2023,** 23, 9091. 10.3390/s23229091
4. Cui, Y. B.; Jiang, J. Analysis on anti-interference performance of sensor in explosive electromagnetic environment. *IEEE Sens. J*. **2024,** 24, 2895-2904. 10.1109/JSEN.2023.3341957
5. Yuan, C.; Wang, Z. Y.; Tang, C. Huang, X.; Y.; Li, Q. A dynamic temperature compensation method for piezoresistive pressure sensors using heat transfer analysis. *IEEE Trans. Instrum. Meas.* **2025,** 74, 2003111. 10.1109/TIM.2025.3545524
6. Kang, J. S.; Yang, S. S. Modeling and experimental evaluation of torque loss in turbine test rig for accurate turbine performance evaluation. *J. Mech. Sci. Technol.* **2012,** 26, 473-479. 10.1007/s12206-011-1031-6
7. Li, Y. X.; Fu, J. Y.; Zhou, Z. F.; Lv, Y. T.; Wan, N.; Chen, D. P. Cosimulation and optimization of constant temperature circuit for thermistor-based MEMS vacuum sensors. *IEEE Sens. J.* **2025,** 25, 21792-21802. 10.1109/JSEN.2025.3564479
8. Zhuang, S. D.; Yang, W.; Zhou, Y. X.; Zou, Y.; Liu, C.; Zhang, L.; Tong, M.; Ma, J. L. Temperature field analysis and compensation improvement of load cell. *Sci. Rep*., **2024,** 14, 26213. 10.1038/s41598-024-76688-0
9. Aryafar, M.; Hamedi, M.; Ganjeh, M. M. A novel temperature compensated piezoresistive pressure sensor. *Measurement*, **2015**, 63, 25–29. 10.1016/j.measurement.2014.11.032

10. Wang, D.; Liu, F. T.; Duan, J. A.; Li, J. H. Temperature compensation study of pressure sensors after leadless packaging. *Sens. Rev.* **2025** 45, 339-347. 10.1108/SR-10-2024-0843
11. Jang, K.; Lee, S.; Lee, J.; Choi, J. Offset-voltage compensation for accurate current-source circuit. *Electron. Lett*. **2012**, 48, 913–914. 10.1049/el.2012.0739
12. Yao, Z.; Liang, T.; Jia, P. G.; Hong, Y. P.; Qi, L.; Lei, C.; Zhang, B.; Xiong, J. J. A high-temperature piezoresistive pressure sensor with an integrated signal-conditioning circuit. *Sensors* **2016**, 16, 913. 10.3390/s16060913
13. Liu, J. W.; Zhang, Z. X.; Wang, Y. H.; Zheng, J. Y.; Guo, Y. Z.; Yao, B.; Zhang, S. Q.; Jing, J. M.; Xu, Y. B.; Xue, C. Y. A board-level temperature compensation method for precise seawater conductivity measurement. *Sens. Actuators A Phys.* **2025**, 388, 116485. 10.1016/j.sna.2025.116485
14. Lei, B. T.; Yi, P. X.; Li, Y. H.; Xiang, J. Y. A temperature drift compensation method for pulsed eddy current technology. *Sensors* **2018**, 18, 1952. 10.3390/s18061952
15. Li, J.; Hu, G. Q.; Zhou, Y. H.; Zou, C.; Peng, W.; Alam, M. S. M. J. A temperature compensation method for piezo-resistive pressure sensor utilizing chaotic ions motion algorithm optimized hybrid kernel LSSVM. *Sensors* **2016**, 16, 1707. 10.3390/s16101707
16. Futane, N. P.; Chowdhury, S. R.; Chowdhury, C. R.; Saha, H. ANN based CMOS ASIC design for improved temperature-drift compensation of piezoresistive micro-machined high resolution pressure sensor. *Microelectron. Reliab.* **2010**, 50, 282-291. 10.1016/j.microrel.2009.09.012
17. Zhang, R.; Duan, Y. F.; Zhao, Y.; He, X. Temperature compensation of elasto-magneto-electric (EME) sensors in cable force monitoring using BP neural network. *Sensors* **2018**, 18, 2176. https: //doi.org/10.3390/s18072176
18. Pang, F. B.; Gu, X. H.; Deng, X.; Chen, Y. X.; Xu, S. Y. Temperature variation mechanism and error suppression of key parameters of phase modulator in fiber optic current sensing system. *Opt. Fiber Technol*. **2024**, 88, 104034. 10.1016/j.yofte.2024.104034
19. Kennedy, J. F.; Eberhart, R.C. Particle swarm optimization. IEEE International Conference on Neural Networks, Perth, WA, Australia, 1995.
20. Gordan, B.; Armaghani, D. J.; Hajihassani, M.; Monjezi, M. Prediction of seismic slope stability through combination of particle swarm optimization and neural network. *Eng. Comput.* **2016**, 32, 85-97. 10.1007/s00366-015-0400-7
21. Wu, J. Q.; Liu, F.; Fan, W. F.; Du, P. C.; Quan, W. Temperature compensation methods of spin-exchange relaxation-free co-magnetometer. *Meas. Sci. Technol.* **2023**, 34, 015113. 10.1088/1361-6501/ac97b0
22. Wang, H.; Zeng, Q. H.; Zhang, Z. Y.; Wang, H. F. Research on Temperature Compensation of Multi-Channel Pressure Scanner Based on an Improved Cuckoo Search Optimizing a BP Neural Network. *Micromachines* **2022**, 13, 1351. 10.3390/mi13081351
23. Yang, X. S.; Deb, S. Cuckoo Search via Levey Flights. In Proceedings of the World Congress on Nature and Biologically Inspired Computing, Co-imbatore, India, 9–11 December 2009.10.1109/NABIC.2009.5393690.
24. Hayyolalam, V.; Kazem, A. A. P. Black Widow optimization algorithm: a novel metaheuristic approach for solving engineering optimization problems. *Eng. Appl. Artif. Intell.* **2020**, 87, 103249. 10.1016/j.engappai.2019.103249.
25. Wang, S. D.; Zhu, W. L.; Shen, Y. J.; Ren, J.; Gu, H. R.; Wei, X. Y. Temperature compensation for MEMS resonant accelerometer based on genetic algorithm optimized backpropagation neural network. *Sens. Actuators A Phys.* **2020**, 316, 112393. 10.1016/j.sna.2020.112393
26. Li, D. P.; Zhang, H. C.; Chen, A.B.; Dong, X.Y.; Yang, Y.; Zheng, D. Z.; Na, R. Adaptive temperature compensation for MoS2 humidity sensor in complex environments using ISSA-BP neural network. *Sens. Actuators A Phys.* **2024**, 379, 115982. 10.1016/j.sna.2024.115982
27. Wang, Q. P.; Li, J. L.; Zhang, S.; Tian, H.; Jie, S. F.; Qu, C. Y.; Liu, Z. C. A novel temperature drift compensation method based on LSTM for NMR sensor. *Measurement.* **2025**, 240, 115573. 10.1016/j.measurement.2024.115573
28. Ding, Y.; Lu, W. K.; Zhang, Y. H.; Feng, Y.; Zhou, Y. Study on the Practical Application of Surface Acoustic Wave Yarn Tension Sensor. *IEEE Trans. Ind. Electron.* **2022**, 69, 13781- 13790. 10.1109/TIE.2021.3135618

29. Hashim, F. A.; Houssein, E. H.; Hussain, K.; Mabrouk, M. S.; Al-Atabany, W. Honey Badger Algorithm: New metaheuristic algorithm for solving optimization problems. *Math. Comput. Simul.* **2022**, 192, 84–110. 10.1016/j.matcom.2021.08.013
30. Wu, T. S.; Chen, S. Y.; Wu, P.; Nie, S. Z. A high precision software compensation algorithm for silicon piezoresistive pressure sensor. *Chin. J. Electron.* **2019**, 28, 748-753. 10.1049/cje.2019.05.001
31. Barthelemy, P.; Bertolotti, J.; Wiersma, D. S. A lévy flight for light. *Nature.* **2008**, 453, 495–498. 10.1038/nature06948
32. Zhang, Z.; Cheng, W. Optimization of a strain gauge load cell using an improved Mayfly algorithm. *Measurement* **2026**, 260, 119855. 10.1016/j.measurement.2025.119855